INTERNATIONAL SOCIETY FOR SOIL MECHANICS AND GEOTECHNICAL ENGINEERING



This paper was downloaded from the Online Library of the International Society for Soil Mechanics and Geotechnical Engineering (ISSMGE). The library is available here:

https://www.issmge.org/publications/online-library

This is an open-access database that archives thousands of papers published under the Auspices of the ISSMGE and maintained by the Innovation and Development Committee of ISSMGE.

The paper was published in the proceedings of the 20th International Conference on Soil Mechanics and Geotechnical Engineering and was edited by Mizanur Rahman and Mark Jaksa. The conference was held from May 1st to May 5th 2022 in Sydney, Australia.

A semi-coupled resolved CFD-DEM method for simulation of thermal-induced phase changes in granular media

Tao Yu & Jidong Zhao

Department of Civil and Environmental Engineering, Hong Kong University of Science and Technology, Hong Kong, China, tyuak@connect.ust.hk

ABSTRACT: We present a semi-coupled Computational Fluid Dynamics (CFD) and Discrete Element Method (DEM) to solve a class of granular media problems that involve thermal-induced phase changes and particle-fluid interactions. We use Immersed Boundary Method to model the viscous fluids surrounding each solid particle in conjunction with a fictious CFD domain occupying the actual position of particle. Heat transfers between the actual fluids and the fictitious particles are solved as a multiphase problem by the CFD only, to resolve the temperature gradient within the particle and its possible phase change (e.g., melting or partial melting). The mechanical interactions between particles and fluids are considered by coupled DEM and CFD in a conventional manner, by considering interaction forces between the DEM and CFD computations. We validated the proposed method with simulations of a typical powder-based selective laser melting process. The simulation results capture key features and observations found in experiments and are quantitatively consistent with existing data. This is part of new research extension of computational granular mechanics.

KEYWORDS: Coupled CFD-DEM method, Immersed Boundary Method, Thermodynamics, Selective Laser Melting.

1 INTRODUCTION

Additive manufacturing (AM), also called 3D printing (3DP), is widely considered a technology paving the way for the next industrial revolution toward the ultimate 'direct digital manufacturing' (DDM) (Berman 2012). It helps eliminate various conventional constraints that hinder optimal design, creativity and ease of manufacturing (Bourell et al. 2009). Among many, selective laser melting (SLM) represents a typical powder-based additive manufacturing technology using highpower lasers to melt metallic powders layer by layer to form a product. It features short manufacturing circle, low costs, better molding accuracy and mechanical properties (Yang et al. 2016), and has seen great potentials for application in a wide range of engineering and industries (Antonysamy 2012, Gowers et al. 2015). Its future developments and wide applications, however, rest on urgent overcoming of a number of technical barriers, including the poor surface roughness control caused by the balling effect, the spatter and "stair step" effect (Strano et al. 2013), and locally poor mechanical properties of built parts (Verhaeghe et al. 2009) caused by pores (Khairallah et al. 2016), cracking, residual stresses, and distortion (Parimi et al. 2014). Both experimental and numerical investigations have been attempted to address these outstanding challenges to advance the SLM technology to a next level (Lian et al. 2018).

Experiments have been primarily focused on examining the effect of various parameters about the powder layer, laser beam and material type, such as laser scanning speed, layer thickness and energy density (Aboulkhair et al. 2014, Ma et al. 2015), aiming to determine appropriate parameters for improving the quality of built parts. However, the qualification process has commonly been laborious and costly as it is featured by empirical trial and error (Mindt et al. 2017). Meanwhile, numerical studies based on different computational methods have been carried out in an attempt to predict the whole manufacturing process and the probability of manufacturing defects (Ganeriwala & Zohdi 2016).

Computational Fluid Dynamics (CFD) is one representative computational method for modeling of SLM (Cook & Murphy 2020) to explain the surface roughness (Wu et al. 2018) and pores (Rausch et al. 2017), including the evolution of temperature and melt pool, and thermo-mechanical effects (Khairallah et al. 2016, Pinkerton 2007) like Recoil pressure, Marangoni's flow and

Plateau-Rayleigh instability. These CFD models can be further divided into two categories according to whether the powder bed is modelled as a continuum medium (King et al. 2015) based on effective thermomechanical properties or discrete packing particles (Cook & Murphy 2020). Recent developments include building a randomly packed powder bed using Discrete Element Method (DEM) (Ganeriwala & Zohdi 2016, Mindt et al. 2017), which has been further coupled with CFD to simulate the powder layering process (Wang et al. 2018) with the effect of ambient gas. However, these studies have not been able to consider particle motion and particle-fluid interactions during the melting process.

In this work, we present a semi-coupled resolved CFD-DEM to solve a class of granular media problems that involve thermalinduced phase changes and particle-fluid interactions during the melting process of SLM. Immersed boundary (IB) method (Shirgaonkar et al. 2009) is used to model the viscous fluids surrounding each solid particle in conjunction with a fictious CFD domain occupying the actual position of particle. Heat transfers between the actual fluids and the fictitious particles are solved as a multiphase problem by the CFD only, to resolve the temperature gradient within the particle and its possible phase change (e.g., melting or partial melting). Mechanical interactions between particles and fluids are considered by coupled DEM and CFD in a conventional manner, by considering interaction forces between the DEM and CFD computations. The numerical model of SLM also considers various physical phenomena like the laser penetration, recoil pressure, Marangoni's flow, and Darcy's effects, and the effects of laser power, laser energy distribution and hatch distance are studied. As will be shown, the simulation results capture key features and observations found in experiments and are reasonably consistent with existing data.

2 METHODOLOGY: COUPLED CFD-DEM

2.1 Two coupled CFD-DEM methods

There are two broad types of coupled CFD-DEM methods developed in the literature, unresolved and resolved CFD-DEM. Unresolved CFD-DEM is a conventional coupled CFD-DEM method with an empirical drag force model (Wang et al. 2019) to evaluate the fluid-particle interactions. In order to meet the requirement of the empirical drag force model and ensure accurate calculations of relative velocity and void fraction, the

grid size should be more than 3 times larger than the particle diameter (Wang et al. 2018). The flow behavior between those particles cannot be resolved as there would be multiple particles in one mesh cell. Therefore, unresolved CFD-DEM offers relatively low resolution and accuracy. It has typically been used to model the powder layering process in SLM.

The resolved CFD-DEM can resolve the microscopic behavior of particles and their surrounding fluids, and can be employed to simulate the melting process in SLM. IB method is a resolved CFD-DEM method, which is developed to resolve the fluid around each particle in an accurate way. It solves fluids and particles separately at first using Direct Numerical Simulation (DNS) and then the fluid-particle interaction is considered by adding a force term derived from the presence of the solid particles to the Navier-Stokes equations, performing a correction of the velocity field of the fluid (Fantin 2018). IB method provides an accurate prediction of the drag force based on the approach published by Shirgaonkar et al. (Shirgaonkar et al. 2009), but its computational cost is much higher than the unresolved CFD-DEM due to the small grid size, which should be smaller than one eighth of the particle diameter (Hager et al. 2014).

2.2 Semi-coupled resolved CFD-DEM method

As the heat transfer and thermal-induced phase change are crucial components in SLM, we propose a semi-coupled resolved CFD-DEM method to predict the accurate thermal field among fluids and particles. In this method, only the dynamics of fluids and motion of particles are solved based on IB method, while the thermal field is solved using a double phase CFD only. A fictious CFD domain occupied by the actual position of particles is created and heat transfers between the actual fluids and the fictitious particle domain are treated as a multiphase problem. If one metallic particle is going to be partially melted, i.e., the temperature of one cell in the particle is higher than the liquidus temperature, it will be deleted in DEM and replaced by high viscous fluids with the same shape in the CFD. Thus, the temperature gradient within the particle and thermal-induced phase change can be resolved.

There are three different phases to be considered during the process, including solid metallic powders in DEM, partially or fully melted metallic powders and the ambient gas in CFD. We employ the volume of fluid (VOF) method to solve this multiphase problem and use volume fraction α_i to represent the existence of different phases in the domain. A new scheme called iso-Advector (Roenby et al. 2016) is used to obtain the complicated surface morphology of the melt flow with ripples, pores, denudation and balling effect. The volume fraction of melt flow and ambient gas is defined as α_1 and α_2 , respectively, where $\alpha_1 + \alpha_2 = 1$. The relationship as well as the density ρ and viscosity μ over the whole domain could be written as ρ = $\alpha_1 \rho_1 + \alpha_2 \rho_2$ and $\mu = \alpha_1 \mu_1 + \alpha_2 \mu_2$. The two parameters will be used in the momentum equation of the fluid. Meanwhile, the void fraction of the particle ε_p will be considered when solving the thermal field. For the value of void fraction ε_p , 1 or 0 means that this cell is inside or outside the DEM particle. The density ρ_T , dynamic viscosity μ_T , thermal conductivity k, heat capacity C used in the temperature equation could be written as (Panwisawas et al. 2017, Wang et al. 2018, Tan et al. 2018b) $\begin{array}{lll} \rho_T = \alpha' \rho_1 + (1-\alpha') \rho_2 &, & \mu_T = \alpha' \mu_1 + (1-\alpha') \mu_2 &, & C = \\ \alpha' \rho_1 C_1 / \rho + (1-\alpha') \, \rho_2 C_2 / \rho & \text{and} & k = \alpha' k_1 + (1-\alpha') k_2 &, \\ \text{where} & \alpha' = (\alpha_1 + 1 - \varepsilon_p). \end{array}$

2.3 Governing Equations

The motion of particles in DEM is governed by the linear and angular momentum equations:

$$m_p \frac{dv_p}{dt} = \mathbf{F}_{\text{drag}} + m_p \mathbf{g} + \sum \mathbf{F}_{p-p} + \sum \mathbf{F}_{p-w}$$
 (1)

$$I_{p}\frac{d\omega_{p}}{dt} = \sum \mathbf{M}_{t} + \sum \mathbf{M}_{r} \tag{2}$$

where m_p and \mathbf{I}_p are the mass and rotational inertia of the particle. \mathbf{g} is the gravitational acceleration. \mathbf{F}_{p-p} and \mathbf{F}_{p-w} are particle-particle interaction force and particle-wall interaction force (Stevens & Hrenya 2005). \mathbf{M}_t and \mathbf{M}_r are the torque from tangential force and rolling friction toque (Zhu et al. 2007). \mathbf{F}_{drag} is the drag force exerted on the particle by surrounding air and metal fluids (Shirgaonkar et al. 2009).

The momentum equation can be written as

$$\begin{split} &\frac{\partial}{\partial t}(\rho \boldsymbol{u}_{f}) + \nabla \cdot (\rho \boldsymbol{u}_{f} \otimes \boldsymbol{u}_{f}) \\ &= -\nabla p_{.rgh} - gh\nabla \rho + \nabla \cdot (\mu \cdot (\nabla \boldsymbol{u}_{f})) \\ &- K_{c} \frac{(\alpha_{1} - \alpha_{m})^{2}}{\alpha_{m}^{3} + C_{k}} \boldsymbol{u}_{f} + c \cdot \sigma \cdot |\nabla \alpha_{1}| \frac{2\rho}{\rho_{1} + \rho_{2}} \boldsymbol{n} \\ &+ 0.54 p_{0} \exp\left(L_{v} \cdot M \frac{T - T_{LV}}{RTT_{LV}}\right) |\nabla \alpha_{1}| \frac{2\rho}{\rho_{1} + \rho_{2}} \boldsymbol{n} \\ &+ \frac{d\sigma}{dT} (\nabla T - \boldsymbol{n}(\boldsymbol{n} \cdot \nabla T)) |\nabla \alpha_{1}| \frac{2\rho}{\rho_{1} + \rho_{2}} \end{split}$$

$$(3)$$

where p_{rgh} is the dynamic pressure, $p_{rgh} = p - \rho g h$, and h is the reference height. K_c is the permeability coefficient, C_k is a constant to avoid division by zero, α_m is the volume fraction of the molten metal which can be approximated using a Gaussian error function (Wang et al. 2018), T_l is the liquidus temperature, T_s is the solidus temperature, c is the curvature, $c=-\nabla \times \mathbf{n}$, **n** the unit normal vector at the interface, $\mathbf{n} = \nabla \alpha_1 / |\nabla \alpha_1|$, σ is the coefficient of surface tension, ρ_m is the density of metal, ρ_g is the density of protective gas, p_0 is the atmospheric pressure, L_{ν} is the latent heat of vaporization, M is the molar mass, T is the temperature, T_{LV} is the boiling temperature, R is the universal gas constant. $|\nabla \alpha_1|$ is an interface term to transform a surface force per unit area into a volumetric surface force (Tan et al. 2018a). $2\rho/(\rho_1+\rho_2)$ is a sharp surface force term to smear out between two phases. $d\sigma/dT$ shows the change of surface tension coefficient with the temperature and it is considered as a material constant in this work.

The last four terms in the RHS of the momentum equation (see Eq. 2) represent the Darcy's effects, surface tension, recoil pressure and Marangoni's flow. During the laser melting process, those partially melted powders are considered as a mushy region with energy dissipation, which is described by the Darcy's term (Rösler & Brüggemann 2011). When the temperature of the metal surface in the melt pool reaches the boiling temperature, evaporation will occur, leading to a recoil pressure on the metal surface, commonly observed as the keyhole phenomena (Tan et al. 2018a). The Marangoni's flow shows the effect of difference in surface tension due to the temperature gradient in the melt pool and its direction is parallel to the tangential direction of the melt flow surface (Cho et al. 2009). These terms are essential to simulate the evolution of various defects and examine their formation mechanism.

The following temperature equation of the melting process is derived from the energy conservation (Panwisawas et al. 2017)

$$\frac{\partial}{\partial t}(C\rho_{T}T) + \nabla \cdot (C\rho_{T}\boldsymbol{u}_{f}T) = S_{l} + \nabla \cdot \nabla(kT)
+ \mu_{T}(\nabla \boldsymbol{u}_{f} + \boldsymbol{u}_{f}\nabla) : \nabla \boldsymbol{u}_{f} - L_{f}\left[\frac{\partial}{\partial t}(\rho_{T}\alpha_{m}) + \nabla \cdot (\rho_{T}\boldsymbol{u}_{f}\alpha_{m})\right]
- h_{c}(T - T_{ref})|\nabla \alpha'| \frac{2C\rho_{T}}{(C_{1}\rho_{1} + C_{2}\rho_{2})}
- \sigma_{sb}(T^{4} - T_{ref}^{4})|\nabla \alpha'| \frac{2C\rho_{T}}{(C_{1}\rho_{1} + C_{2}\rho_{2})}
- 0.82 \frac{L_{v} \cdot M \cdot p_{0}}{(2\pi MRT)^{0.5}} \exp\left(L_{v} \cdot M \frac{T - T_{LV}}{RTT_{LV}}\right)|\nabla \alpha'| \frac{2C\rho_{T}}{(C_{1}\rho_{1} + C_{2}\rho_{2})}$$

where S_l is the laser input, $\alpha' = (\alpha_1 + 1 - \partial_p)$, L_f is the latent heat of fusion, h_c is the convective heat transfer coefficient, T_{ref} is the reference temperature, σ_{sb} is the Stefan-Boltzmann constant. $2C\rho_T/(C_1\rho_1 + C_2\rho_2)$ is also a sharp surface force term to smear out between two phases. The last six terms (Wang et al. 2018) in Eq. 3 represent the heat transfer due to conduction, dissipation, fusion, convection, radiation, and evaporation. The laser source term S_l can be written as

$$S_l = \frac{f_{\text{absorb}}}{\Lambda L} Q_{l,S} \tag{5}$$

$$(f_{\text{absorb}})_{\text{cell}I} = \alpha' (e^{-\gamma z_1} - e^{-\gamma z_2})_{\text{cell}I}$$
 (6)

$$Q_{l,S} = \frac{2P}{\pi R'^2} exp \left[\frac{-2\left[\left(x - X_l(t) \right)^2 + \left(y - Y_l(t) \right)^2 \right]}{{R'}^2} \right]$$
(7)

where $f_{\rm absorb}$ is the laser absorption coefficient based on the general Beer-Lambert form, which reflects an exponential decay through the powder bed (Mukherjee et al. 2016), z_1 and z_2 are the depths of this cell's top side and bottom side in the powder layer, g is the attenuation coefficient (McVey et al. 2007), P is the laser power, $R'^2 = R_0^2 + [\lambda (z - z_f)/\pi R_0]^2$, R_0 is the laser beam radius, z_f is the z-coordinate of the lens focus, λ is the wave length of the laser, (x,y,z) is the coordinate of the cell, $(X_l(t), Y_l(t))$ represents the center of the scanning path in the x-y plane.

Various models for calculating the absorption coefficient have been proposed and developed (Panwisawas et al. 2017, Wang et al. 2018, Tan et al. 2018b), but the reflection and transmission of the laser are not considered in these models. In this work, if metallic powders are not melted, the initial attenuation coefficient y_1 in the absorption coefficient is determined based on the experiment given by McVey (McVey et al. 2007). When metallic powders begin to melt, the molten flow could be easily heated over the boiling point (Matthews et al. 2016), so we assume that the surface of molten pool would absorb most of the laser energy if the liquidus metal begins to evaporate. In previous absorption coefficient models, only the upper three or four cell layers (interface) of the metal phase can absorb the laser energy. In this work, the upper four cell layers of the metal will absorb most (99%) of the laser energy when reaching the fully melting, which means that $(1 - e^{-\gamma_2 \cdot 4\Delta L}) \ge$ 0.99, then the value of γ_2 can be solved. The attenuation coefficient between these two conditions is approximated using a Gaussian error function,

$$\gamma = \gamma_1 + \frac{\gamma_2 - \gamma_1}{2} \left[1 + \operatorname{erf}\left(\frac{4}{T_{LV} - T_l} \left(T - \frac{T_{LV} + T_l}{2}\right)\right) \right] \tag{8}$$

The temperature field will be updated after solving Eq. 3 and if the temperature of one cell in one particle is higher than the liquidus temperature, this particle will be deleted in DEM and replaced by spherical fluid with a high solidus viscosity μ_s in CFD. This solidus viscosity will decrease to liquidus viscosity μ_t when the temperature reaches the liquidus point. There are some models (Wang et al. 2018, Tan et al. 2018b, Chris 2017) to approximate the viscosity transition from the solidus temperature to liquidus temperature, and the model used in this work is proposed by Wang (Wang et al. 2018) as it can obtain a viscosity with upper and lower limits, given by

$$\ln \mu_1 = \text{erfc} \left[\frac{2(2 \ln T - \ln(T_l T_s))}{\ln T_l - \ln T_s} \right] \frac{(\ln \mu_s - \ln \mu_l)}{2} + \ln \mu_l$$
 (9)

where μ_s and μ_l are the viscosities at solidus temperature and liquidus temperature, erfc is the complementary Gaussian error function.

2.4 Solution procedures

The solution algorithm of this semi-coupled CFD-DEM method is described as follows (see Figure 1):

- Prescribe the initial or last time step conditions for both CFD and DEM, including the temperature field, pressure field, velocity field of fluids and the velocity, position of particles.
- (2) Calculate the drag force acting on the particles and update the particle motion using the Newton's Second Law of Motion with a particle collision model (Zhou et al. 2010). The temperature of each cell in the domain of particles will be checked. The particle will be deleted in DEM if the temperature of its cell is higher than the solidus temperature, indicating that the powder is partially melted.
- (3) Verify the change of void fraction field to identify whether the particle is deleted, and those deleted particles are replaced by fluids with the same temperature by changing the volume fraction field. Update all related parameters according to the new volume fraction field and temperature field, including the density, heat capacity, thermal conductivity and viscosity.
- (4) Update the laser source coefficient firstly based on the position of particles and fluids and the temperature field, and then by calculating the temperature equation in CFD, where the laser source, three heat transfer terms including conduction, convection and radiation, and the enthalpy change due to fusion and evaporation are considered.
- (5) Calculate the volume fraction of metal and protective gas and reconstruct the surface of melt flow using iso-Advector method. Update all the related parameters according to the new volume fraction field and temperature field, including the density, heat capacity, thermal conductivity and viscosity.
- (6) Update the velocity field and pressure field by solving velocity equation and pressure equation, where the buoyancy force, Darcy's effects, surface tension, Marangoni's flow, recoil pressure are considered. Correct the velocity field and pressure field of fluids according to IB Method.
- Return to step (2) to repeat the simulation until reaching the final time step.

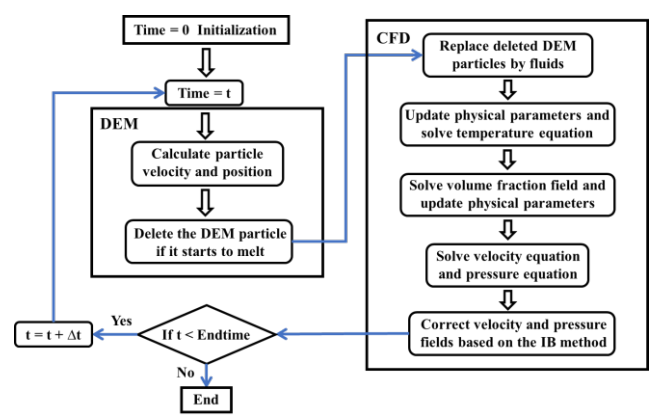


Figure 1. Flow chat of the semi-coupled resolved CFD-DEM method

3 NUMERICAL SIMULATION

3.1 Model Setup and Parameter Selection

In this work, the melting process of a typical titanium alloy Ti-6Al-4V is studied and relevant physical parameters (Tan et al. 2018b) are shown in Table 1.

Table 1. Physical parameters of the numerical model

Parameter Parameter	Value and units	Parameter	Value and units
Liquidus temperature	1923K	Solidus temperature	1878K
Boiling temperature	3133K	Laser Diameter	140µm
Initial temperature	300K	Laser velocity	60cm/s
Initial attenuation coefficient	0.0144	Air density	$1 kg/m^3$
Latent heat of fusion	$\begin{array}{c} 2.88{\times}10^{5} \\ m^{2}/s^{2} \end{array}$	Molar mass	446.07 g/mol
Latent heat of evaporation	$4.7 \times 10^{6} \\ m^{2}/s^{2}$	Atmospheric pressure	101000 Pa
Change rate of surface tension coefficient	-2.6×10^{-4} kg/(s ² ·K)	Surface tension coefficient at melt point	1.5 kg/ s^2
Convective heat transfer coefficient	19 kg⋅s³⋅K	Viscosity of air	1.5×10^{-5} m ² /s
Viscosity of liquid Ti-6Al-4V alloy	0.005 Pa·s	Heat capacity of air	$\frac{1164}{m^2/(s^2 \cdot K)}$

As mentioned by (Wang et al. 2018), it is more physical to consider the temperature-dependent parameters, while those thermal parameters are usually set as constants in commercial software. According to American Society for Metals (ASM) (Valencia & Quested 2008), the density ρ , heat capacity C, thermal conductivity k of Ti-6Al-4V alloy can be approximated as

$$\rho \atop (kg/m^3) = \begin{cases} 4420 & T < 1268K \\ 4420 - 0.154(T - 298) & 1268K < T < 1923K \\ 3920 - 0.680(T - 1923) & T \ge 1923K \end{cases}$$

$$C \atop (m^2/(s^2K)) = \begin{cases} 411.5 & T < 1268K \\ 411.5 + 0.2T + 5 \times 10^{-7}T^2 & 1268K < T < 1923K \\ 830 & T \ge 1923K \end{cases}$$

$$k \atop (W/(mK)) = \begin{cases} 19.0 & T < 1268K \\ -0.797 + 0.018T - 2 \times 10^{-6}T^2 & 1268K < T < 1923K \\ 33.4 & 1923K < T < 1973K \\ 34.6 & T > 1973K \end{cases}$$

$$(10)$$

The chosen viscosity at solidus temperature μ_s is crucial for the accuracy of simulation results. An extremely high viscosity may help to guarantee that the movement of those fluids are close to the solid powders and the Deborah Number could be much larger than 1 (Reiner 1964). One experiment (Nandan et al. 2008) shows that the viscosity μ_s of Ti-6Al-4V alloy is larger than $10^{7.5}$ Pa s at low strain rate (<10s⁻¹), which is nearly 6×10^9 times larger than m_l (0.005Pa·s). However, such a large μ_s requires extremely large number of PISO correction iterations to achieve the phase fraction and pressure convergence (Silva & Lage 2011). In this work, in order to satisfy the equilibrium between efficiency and accuracy, a relatively small viscosity is approximated as 1.41 Pa·s, which can guarantee that the Deborah Number is much larger than 1 and the required number of iterations can drop to a normal level to reduce total CPU time (Frederix et al. 2015). The radius of particles in the model is ranged from 9 µm to 28 µm, and its size distribution is the same as the powder size distribution of Ti-6Al-4V measured by (Panwisawas et al. 2017) using a laser diffraction particle size analyzer. The mean diameter is around 36 μ m, nine times the length of grid size (Yu & Zhao 2021) (4 μ m).

3.2 Validation with experimental data

In this section, the multiscale prediction for SLM based on the proposed semi-coupled resolved CFD-DEM is validated against experimental data. Specifically, two groups of cases in terms of different laser power and hatch distance of multiple tracks are considered in this validation section.

Figure 2 shows the Marangoni driven ripples and piled trackheads observed in the experiment performed by (Trapp et al. 2017) in comparison with our simulations where the simulated ripples are highlighted in yellow dashed lines. Marangoni effect is one type of flow instability, caused by the large fluid temperature gradient and the induced change of surface tension. As the surface tension will decrease with the increasing temperature for Ti-6Al-4V alloy, the low temperature molten flow behind the laser spot has a higher surface tension, further driving the molten pool flowing back and forming the ripples due to quick solidification. In this simulation, the scanning speed is 60 cm/s and three laser powers, namely, 150W, 200W and 300W, are used. Evidently, the ripples become larger and sharper when the laser power grows due to larger molten pool and temperature gradient. The increase in laser power also leads to inhomogeneous ripples. When the laser power is low, the energy is not sufficient to form ripples in some region. If the laser power is very high, larger molten pool, temperature gradient and recoil force will lead to the combination of close ripples, increasing the thickness, size and interval of final ripples. These phenomenon are consistent with the experimental results (Trapp et al. 2017) shown in Figure 2 (d).

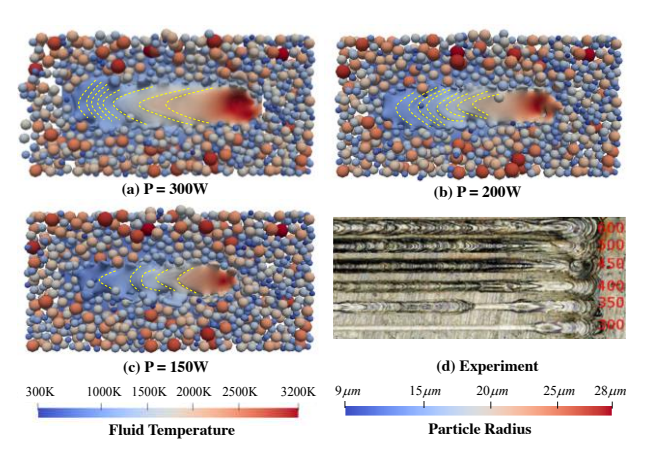
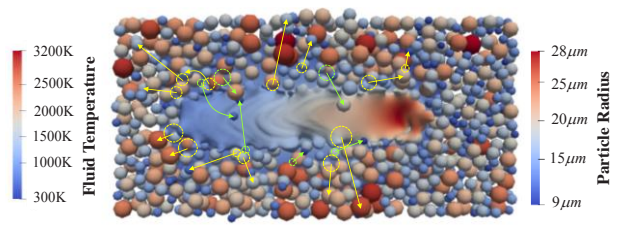
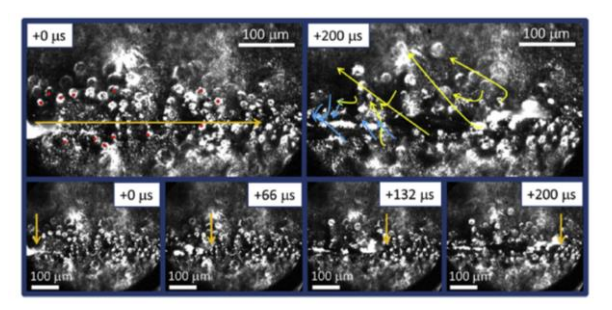


Figure 2. Simulation and experimental results with different laser power

As DEM is coupled in this numerical method, the powder movement can be solved during the melting process in the study. The vapor recoil and spatially varying absorptivity (Kaplan 2012) is the primary cause of the powder movement, which can result in the localized fluid flow, further interacting with the surrounding powders (Matthews et al. 2016). The high speed imaging (Matthews et al. 2016) illustrating the powder movement in experiment and the related simulation result are shown in Figure 3, which demonstrate the similar powder movement. Yellow arrow trajectories represent powders swept away from the molten pool and other arrow trajectories represent powders colliding with the molten pool. This phenomenon is driven by the vertical momentum from particle-particle collisions, causing scattered downward movement for some powders (Matthews et al. 2016). Vapor is also a dominant factor for the powder movement but has not been considered in this study.



(a) Simulation result of typical powder movement (200W)



(b) High speed imaging of molten track progression and powder movement (Matthews et al. 2016)

Figure 3. Simulation and experimental results of powder movement during melting process

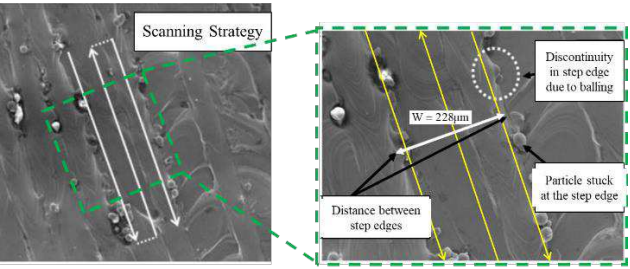


Figure 4. Experimental result of three overlapped scan tracks (Strano et al. 2013)

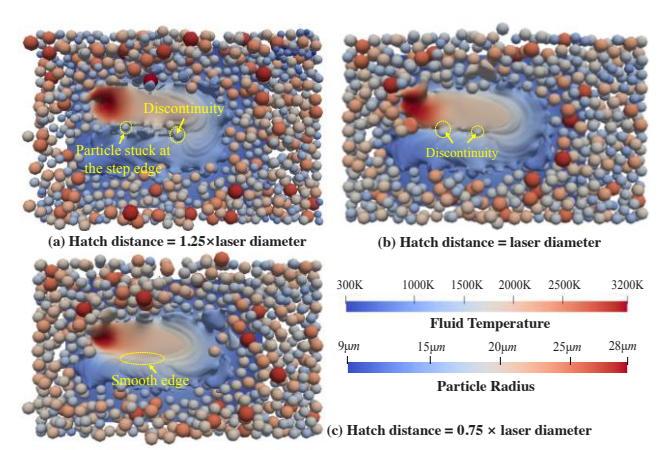


Figure 5. Simulation results of multi-track model

The hatch distance is a dominant factor in a multi-track model, controlling the manufacturing efficiency and surface quality. Figure 4 illustrates the surface quality of multiple molten tracks (Strano et al. 2013) and discontinuity as well as sticking particles can be found in step edge, increasing the surface roughness. This defect may be eliminated by using the scanning strategy with overlapped scan tracks. For example, A 25% scan overlap can effectively decrease the discontinuity at the step edge (Thijs et al. 2010), reaching a higher Vickers microhardness value of final samples. This phenomenon can be also discovered

in three multi-track numerical models (Figure 5) with different hatch distances equal to 125%, 100% and 75% of the laser diameter. If the hatch distance equals laser diameter, sticking particles can be eliminated but the discontinuity due to balling effect can be still found in the simulation result, which further demonstrates the critical role of overlapped scan tracks.

4 CONCLUSIONS

A semi-coupled resolved CFD-DEM method has been proposed to solve a class of granular media problems that involve thermal-induced phase changes and particle-fluid interactions. The method is validated by modelling a typical powder-based selective laser melting (SLM) process, and the effect of laser power and hatch distance is discussed. The simulation results capture key features and observations found in experiments and are quantitatively consistent with existing data. Major conclusions drawn from the study are summarized as follows:

- (a) The semi-coupled resolved CFD-DEM method is feasible for simulated powder-based SLM. It features an IB Method to model the viscous fluids surrounding each solid particle in conjunction with a fictious CFD domain occupying the actual position of particle. Heat transfers between the actual fluids and the fictitious particles are solved as a multiphase problem by the CFD only, whereas the particle-fluid interactions are solved by coupled DEM and CFD. The proposed method can resolve the motion of powders, dynamics of molten flow and powder-flow interaction, providing a rational basis for further optimization of SLM.
- (b) Three phases, including the ambient gas, solid metallic powders and molten flow are fully built in the proposed method for modeling melting process. The combination of the iso-Advector method and IB Method helps to obtain accurate molten surface and particle-fluid interactions. Simulation results with different laser power and hatch distance illustrate crucial phenomena in SLM, such as the typical powder motion, ripples of single molten track and surface quality of multiple tracks, validating this numerical method.
- (c) Laser power can affect the printed surface quality greatly. A low laser power would cause lateral pores and discontinuity due to partially melted powders, leading to a rough molten surface. If the laser power is too high, surface roughness may increase due to the larger and sharper ripples. For multi-track melting, an overlap between two molten tracks is necessary to improve the surface quality and eliminate the discontinuity and sticking particles in the track edge. During the melting process, some particles may collapse and collide with the molten track and others may be ejected away due to the recoil pressure and Marangoni effect, which will further affect neighboring tracks.

5 ACKNOWLEDGEMENTS

The study is financially supported by HKUST-FP907 and F-HKUST601/19. The first author acknowledges the sponsorship of Hong Kong Ph.D. Fellowship offered by Research Grants Council of Hong Kong on his study.

6 REFERENCES

Aboulkhair, N. T., N. M. Everitt, I. Ashcroft, and C. Tuck. 2014. Reducing porosity in AlSi10Mg parts processed by selective laser melting. Additive Manufacturing 1, 77-86.

Antonysamy, A. A. 2012. Microstructure, Texture and Mechanical Property Evolution during AdditiveManufacturing of Ti6Al4V Alloy for Aerospace Applications, The University of Manchester (United Kingdom).

- Berman, B. 2012. 3-D printing: The new industrial revolution. *Business horizons* 55 (2), 155-162.
- Bourell, D. L., M. C. Leu, and D. W. Rosen. 2009. Roadmap for additive manufacturing: identifying the future of freeform processing. *The University of Texas at Austin, Austin, TX*, 11-15.
- Cho, J.-H., D. F. Farson, J. O. Milewski, and K. J. Hollis. 2009. Weld pool flows during initial stages of keyhole formation in laser welding. *Journal of Physics D: Applied Physics* 42 (17), 175502.
- Chris, G. 2017. 7.1 Thermophysical models, OpenFOAM v5 user guide. London: OpenFOAM Foundation.
- Cook, P. S., and A. B. Murphy. 2020. Simulation of melt pool behaviour during additive manufacturing: Underlying physics and progress. *Additive Manufacturing* 31, 100909.
- Fantin, D. 2018. CFD-DEM Coupling for Systems of Fluid and Non-Spherical Particles, Delft University of Technology, Delft
- Frederix, E., M. Stanic, A. K. Kuczaj, M. Nordlund, and B. J. Geurts. 2015. Extension of the compressible PISO algorithm to singlespecies aerosol formation and transport. *International Journal of Multiphase Flow* 74, 184-194.
- Ganeriwala, R., and T. I. Zohdi. 2016. A coupled discrete element-finite difference model of selective laser sintering. *Granular Matter* 18 (2), 21.
- Gowers, S. A., V. F. Curto, C. A. Seneci, C. Wang, S. Anastasova, P. Vadgama, G.-Z. Yang, and M. G. Boutelle. 2015. 3D printed microfluidic device with integrated biosensors for online analysis of subcutaneous human microdialysate. *Analytical chemistry* 87 (15), 7763-7770.
- Hager, A., C. Kloss, S. Pirker, and C. Goniva. 2014. Parallel resolved open source CFD-DEM: method, validation and application. *The Journal of Computational Multiphase Flows* 6 (1), 13-27.
- Kaplan, A. F. 2012. Local absorptivity modulation of a 1 μm-laser beam through surface waviness. Applied Surface Science 258 (24), 9732-9736
- Khairallah, S. A., A. T. Anderson, A. Rubenchik, and W. E. King. 2016. Laser powder-bed fusion additive manufacturing: Physics of complex melt flow and formation mechanisms of pores, spatter, and denudation zones. *Acta Materialia* 108, 36-45.
- King, W. E., A. T. Anderson, R. M. Ferencz, N. E. Hodge, C. Kamath, S. A. Khairallah, and A. M. Rubenchik. 2015. Laser powder bed fusion additive manufacturing of metals; physics, computational, and materials challenges. *Applied Physics Reviews* 2 (4), 041304.
- Lian, Y., S. Lin, W. Yan, W. K. Liu, and G. J. Wagner. 2018. A parallelized three-dimensional cellular automaton model for grain growth during additive manufacturing. *Computational Mechanics* 61 (5), 543-558.
- Ma, M., Z. Wang, M. Gao, and X. Zeng. 2015. Layer thickness dependence of performance in high-power selective laser melting of 1Cr18Ni9Ti stainless steel. *Journal of Materials Processing Technology* 215, 142-150.
- Matthews, M. J., G. Guss, S. A. Khairallah, A. M. Rubenchik, P. J. Depond, and W. E. King. 2016. Denudation of metal powder layers in laser powder bed fusion processes. *Acta Materialia* 114, 33-42.
- McVey, R., R. Melnychuk, J. Todd, and R. Martukanitz. 2007. Absorption of laser irradiation in a porous powder layer. *Journal of Laser Applications* 19 (4), 214-224.
- Mindt, H., O. Desmaison, and M. Megahed. 2017. Modelling Powder Bed Additive Manufacturing Defects. In *Proc 7th European* Conference for Aeronautics and Space
- Sciences, 1-6.
- Mukherjee, T., J. Zuback, A. De, and T. DebRoy. 2016. Heat and fluid flow modeling to examine 3D-printability of alloys. Paper read at 7th International Symposium on High-Temperature Metallurgical Processing.
- Nandan, R., T. Lienert, and T. DebRoy. 2008. Toward reliable calculations of heat and plastic flow during friction stir welding of Ti-6Al-4V alloy. *International Journal of Materials Research* 99 (4), 434-444.
- Panwisawas, C., C. Qiu, M. J. Anderson, Y. Sovani, R. P. Turner, M. M. Attallah, J. W. Brooks, and H. C. Basoalto. 2017. Mesoscale modelling of selective laser melting: thermal fluid dynamics and microstructural evolution. *Computational Materials Science* 126, 479-490.
- Parimi, L. L., G. Ravi, D. Clark, and M. M. Attallah. 2014. Microstructural and texture development in direct laser fabricated IN718. *Materials Characterization* 89, 102-111.
- Pinkerton, A. J. 2007. An analytical model of beam attenuation and

- powder heating during coaxial laser direct metal deposition. *Journal of Physics D: Applied Physics* 40 (23), 7323.
- Rausch, A. M., V. E. Küng, C. Pobel, M. Markl, and C. Körner. 2017. Predictive simulation of process windows for powder bed fusion additive manufacturing: Influence of the powder bulk density. *Materials* 10 (10), 1117.
- Reiner, M. 1964. The deborah number. Physics today 17 (1), 62.
- Roenby, J., H. Bredmose, and H. Jasak. 2016. A computational method for sharp interface advection. Royal Society open science 3 (11), 160405.
- Rösler, F., and D. Brüggemann. 2011. Shell-and-tube type latent heat thermal energy storage: numerical analysis and comparison with experiments. *Heat and Mass Transfer* 47 (8), 1027.
- Shirgaonkar, A. A., M. A. MacIver, and N. A. Patankar. 2009. A new mathematical formulation and fast algorithm for fully resolved simulation of self-propulsion. *Journal of Computational Physics* 228 (7), 2366-2390.
- Silva, L. F. L., and P. L. Lage. 2011. Development and implementation of a polydispersed multiphase flow model in OpenFOAM. Computers & Chemical Engineering 35 (12), 2653-2666.
- Stevens, A. B., and C. Hrenya. 2005. Comparison of soft-sphere models to measurements of collision properties during normal impacts. *Powder technology* 154 (2-3), 99-109.
- Strano, G., L. Hao, R. M. Everson, and K. E. Evans. 2013. Surface roughness analysis, modelling and prediction in selective laser melting. *Journal of Materials Processing Technology* 213 (4), 589-597.
- Tan, J., C. Tang, and C. Wong. 2018a. Study and modeling of melt pool evolution in selective laser melting process of SS316L. MRS Communications 8 (3), 1178-1183.
- Tan, J. L., C. Tang, and C. H. Wong. 2018b. Study and modeling of melt pool evolution in selective laser melting process of SS316L. MRS Communications 8 (03), 1178-1183.
- Thijs, L., F. Verhaeghe, T. Craeghs, J. V. Humbeeck, and J.-P. Kruth. 2010.
 A study of the microstructural evolution during selective laser melting of Ti–6Al–4V. Acta Materialia 58 (9), 3303-3312.
- Trapp, J., A. M. Rubenchik, G. Guss, and M. J. Matthews. 2017. In situ absorptivity measurements of metallic powders during laser powder-bed fusion additive manufacturing. *Applied Materials Today* 9, 341-349.
- Valencia, J. J., and P. N. Quested. 2008. Thermophysical properties, ASM Handbook. Vol. 15: ASM International.
- Verhaeghe, F., T. Craeghs, J. Heulens, and L. Pandelaers. 2009. A pragmatic model for selective laser melting with evaporation. *Acta Materialia* 57 (20), 6006-6012.
- Wang, Z., K. Walayat, and M. Liu. 2019. A velocity corrected unresolved CFD-DEM coupled method to reproduce wake effects at moderate Reynolds number. *Engineering Computations*.
- Wang, Z., W. Yan, W. K. Liu, and M. Liu. 2018. Powder-scale multiphysics modeling of multi-layer multi-track selective laser melting with sharp interface capturing method. *Computational Mechanics* 63 (4), 649-661.
- Wu, Y.-C., W.-S. Hwang, C.-H. San, C.-H. Chang, and H.-J. Lin. 2018. Parametric study of surface morphology for selective laser melting on Ti6Al4V powder bed with numerical and experimental methods. *International Journal of Material Forming* 11 (6), 807-813.
- Yang, Y., Y. Chen, Y. Wei, and Y. Li. 2016. 3D printing of shape memory polymer for functional part fabrication. *The International Journal* of Advanced Manufacturing Technology 84 (9-12), 2079-2095.
- Yu, T., and J. Zhao. 2021. Semi-coupled resolved CFD–DEM simulation of powder-based selective laser melting for additive manufacturing. Computer Methods in Applied Mechanics and Engineering 377, 113707.
- Zhou, Z., S. Kuang, K. Chu, and A. Yu. 2010. Discrete particle simulation of particle–fluid flow: model formulations and their applicability. *Journal of Fluid Mechanics* 661, 482-510.
- Zhu, H., Z. Zhou, R. Yang, and A. Yu. 2007. Discrete particle simulation of particulate systems: theoretical developments. *Chemical Engineering Science* 62 (13), 3378-3396.